

Experimental study of z resolution in Acousto-Optical Coherence Tomography using random phase jumps on ultrasound and light

Max Lesaffre¹, Salma Farahi², Franois Ramaz¹ and Michel Gross³

¹*Institut Langevin, ESPCI ParisTech, CNRS UMR 7587, 1, rue Jussieu F-75238 Paris Cedex 05.*

²*School of Engineering, Ecole Polytechnique Federale de Lausanne (EPFL), Station 17, CH-1015 Lausanne, Switzerland .*

³*Laboratoire Charles Coulomb- UMR 5221 CNRS-UM2 Université Montpellier II place Eugène Bataillon 34095 Montpellier*

Compiled April 30, 2022

Acousto-Optical Coherence Tomography (AOCT) is a variant of Acousto Optic Imaging (also called Ultrasound modulated Optical Tomography) that makes possible to get resolution along the ultrasound propagation axis z . We present here new AOCT experimental results, and we study how the z resolution depends on time step between phase jumps T_ϕ , or on the correlation length Δz . By working at low resolution, we perform a quantitative comparison of the z measurements with the theoretical Point Spread Function (PSF). We present also images recorded with different z resolution, and we qualitatively show how the image quality varies with T_ϕ , or Δz . © 2022 Optical Society of America

OCIS codes: 170.3660, 110.7050, 110.7170, 160.5320, 170.3880

1. Introduction

Citation:

Max Lesaffre, Salma Farahi, Franois Ramaz and Michel Gross "Experimental study of z resolution in Acousto-Optical Coherence Tomography using random phase jumps on ultrasound and light" Applied Optics: **52**,5, pp. 949 - 957 (2013)

Acousto-optic imaging (AOI) [1–5] combines light and ultrasounds to measure local optical properties through thick and highly scattering media.

The principle of this imaging method is the following. Ultrasound (US) is applied in the region of interest, within the thick scattering sample, making the scatterers vibrate. A CW laser illuminates the sample. The vibration of the scatterers at the acoustic US frequency ω_{US} (2MHz typically) modulates the phase of the photons that are scattered by the sample. The light exiting the sample contains thus different frequency components. The main component (carrier) is centered at the laser illumination frequency ω_L . It is related to the scattered photons, that do not interact with the US. The sideband components at frequencies $\omega_{\pm 1}$ are shifted from the US frequency so that $\omega_{\pm 1} = \omega_L \pm \omega_{US}$. The sideband photons, which result from the interaction between light and US, are called "tagged photons", their weight depends on the optical absorption in the region of interest, where the US beam is focused. Acousto-optic imaging detects selectively the tagged photons. The signal is recorded while scanning the US within the volume of the sample, and thus one gets informations of the local optical absorption and/or scattering in 2D or 3D.

The first experiments were performed with fast single detectors to record the modulation of the optical signal at the US frequency [1–3, 5, 6], but, since the phase of

the modulation is different for each grain of speckle, the detector can only process one grain of speckle. In order to increase the optical etendue of detection, Leveque et al. [4] have developed a camera coherent detection technique that processes many speckles in parallel. This technique has been pulled to the photon shot noise limit by Gross et al. [7] using a holographic heterodyne technique [8] able to detect photons with optimal sensitivity [9, 10]. But, because of the tissue inner motions, the frequency bandwidth of the photons that travel through living tissue is enlarged (1.5 kHz typically through 4 cm of living breast tissue [11]), while the bandwidth of the camera coherent detection ($1/T$) is limited by the exposure time T . In order to increase this bandwidth, one has to decrease T , and thus the detected signal remains almost the same. This means that the detected signal is essentially independent of camera exposure time T , if this time T is longer than correlation time of the sample speckle. This point has been experimentally demonstrated with turbid liquid [12]. An alternative to match the detection and the signal bandwidth while keeping a large optical etendue is to use a detection involving a detection bandwidth comparable with the signal bandwidth while keeping a large optical etendue, is to use a detection schemes involving photorefractive (PR) crystals [13–17].

Since the US attenuation is low in tissues, tagged photons are generated along the US propagation z axis at nearly constant rate. This means that in a continuous regime of the US, the AO techniques give nearly no information on the location of the embedded objects along the z axis. In order to get z information, acoustic pulses can be used whether with single detectors [18, 19], cameras [20] and PR crystals [13–16, 21, 22]. Nevertheless, reaching a millimetric resolution with US pulses requires

a typical duty cycle of 1%, corresponding to the ratio of the exploration length within the sample (~ 10 cm) and the desired resolution (~ 1 mm). This is problematic regarding the very small quantity of light that emerges from a clinical sample, since a weak duty cycle yields a low signal and a poor SNR.

In a recent publication, Lesaffre et al. [23] overcome the duty cycle problem, and get z resolution with a variant of the acousto optic technique, called Acousto Optical Coherence Tomography (AOCT). In this technique, the same random phase modulation is applied on both light and US, but the light modulation is applied at retarded time $t + z/c_{US}$, where z is the coordinate of the selected zone, and c_{US} the US velocity. The Lesaffre et al. experiment has been made with PR detection of the tagged photon signal, and, in that case, the exact shape of the z instrumental response has been calculated [24].

In this paper, we will present new experimental results in order to verify this theory by studying how the z resolution depends on the characteristic time of the random phase jumps, T_ϕ . We will recall briefly the theoretical results of reference [24], and introduce the AOCT resolution Δz . By working at low resolution, we will perform a quantitative comparison of the measured z shape, with the theoretical one. We will then present images recorded with different resolution Δz , and qualitatively show how the images quality varies with Δz .

2. The experimental setup

The experimental setup is presented on Fig.1. It is close to the one described elsewhere [23]. An acoustic transducer (Panametrics A395S-SU, focal length of 75 mm) generates a US beam, which is focused on the sample (frequency $\omega_{US} = 2.3$ MHz, with a maximum US pressure $P_{US} \simeq 1.6$ MPa at the focal point). The master laser (wavelength $\lambda = 1064$ nm, 5 W after amplification) is spatially single mode (transverse and longitudinal) and vertically polarized. It is splitted in two beams, whose amplitude, phase and frequency are controlled by two acousto optic modulators (AOM1 and AOM2) driven at $\omega_{AOM1} \simeq \omega_{AOM2} = 80$ MHz. The first beam illuminates the sample (area $s \sim 1$ cm²). Note that the output signal beam is totally depolarized because of the multiple diffusion events in the scattering sample. The second (reference) pumps the photorefractive (PR) crystal. The relative power of the reference versus illumination beam is adjusted by a half wave plate ($\lambda/2$) followed by a polarizing beam splitter (BS). The PR crystal is a bulk GaAs crystal ($1.4 \times 1.6 \times 1.4$ cm³ [23]), oriented into an anisotropic diffraction configuration [22, 25]. The signal beam, which is depolarized, and the reference beam, which is vertically polarized, enter onto orthogonal faces, respectively $(11\sqrt{2})$ and $(\overline{11}\sqrt{2})$, in order to have a grating vector along $\langle 001 \rangle$. In such a configuration, the effective electro optic coefficient is $r_{eff} = r_{41}$. A polarizer oriented at $\pi/4$ relative vertical is positioned after the sample, while a horizontally oriented polarizer is po-

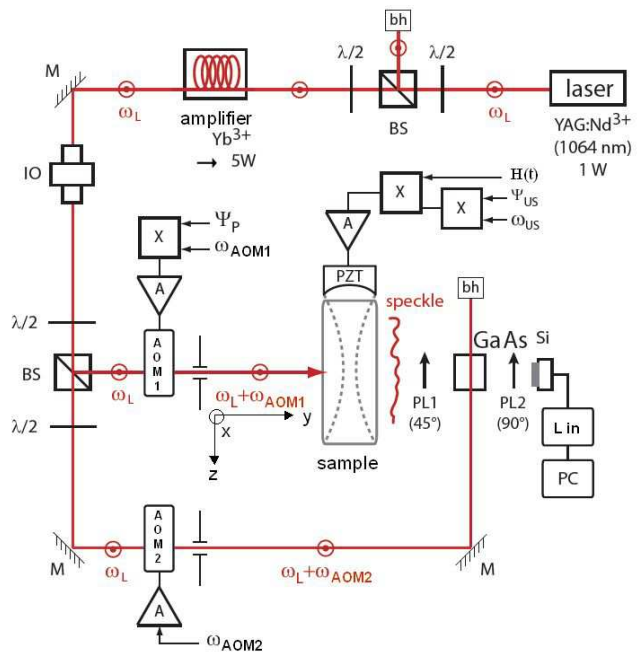


Fig. 1. AOCT experimental setup. Laser: Nd: YAG laser (1 W @ 1064nm); amplifier: optical amplifier 5W-doped Yb; IO: optical isolator Faraday; $\lambda/2$: half-wave plate; AOM1, 2: acousto optic modulators; M: mirror; BS: polarizing beam splitter; X : Radio Frequency (RF) ~ 80 MHz Double Balanced Mixer; A: RF amplifier; GaAs: photorefractive GaAs crystal; PL1,2: linear polarizers; Si: Silicon photodiode (0.3 cm²); L in: Lock-In amplifier; PC: personal computer; PZT: Piezoelectric acoustic transducer (~ 2 MHz). $H(t)$: 0, π random phase modulation at frequency $\omega_{mod} = 3$ kHz, and with duty cycle $r = 0.24$; ψ_{US} , ψ_P : random sequence of phase.

sitioned after the crystal. This configuration minimizes scattering of the intense reference beam by the PR crystal, which corresponds to the main parasitic light contribution. For a typical reference beam of power $P_R = 650$ mW over an area $S_R = 0.32$ cm², the photorefractive response time is $\tau_{PR} = 3.4$ ms.

In order to perform the z axis selection of the tagged photons, the phases of illumination ($\psi_P(t)$) and US ($\psi_{US}(t)$) beams are pseudo-randomized. Every time interval T_ϕ , we apply pseudo random phase jumps of 0 or π on both illumination and US (i.e. we multiply the corresponding sinusoidal signal by either +1 or -1 every T_ϕ). By using two DBM (Double Balanced Mixers ZAD-1H: Mini-Circuits Lab. Inc.), the sine wave signals of frequency ω_{AOM1} and ω_{US} that drive the acousto optic modulator AOM1 and the PZT transducer are mixed with two correlated rectangular pseudo random phase signals $e^{j\psi_P(t)} = \pm 1$ and $e^{j\psi_{US}(t)} = \pm 1$. These pseudo random signals are generated by two 80 MHz arbitrary waveform generators (Agilent 33250A) with a common 10 MHz reference clock. Because of the finite memory (N words) of the generators, the phase signals, which

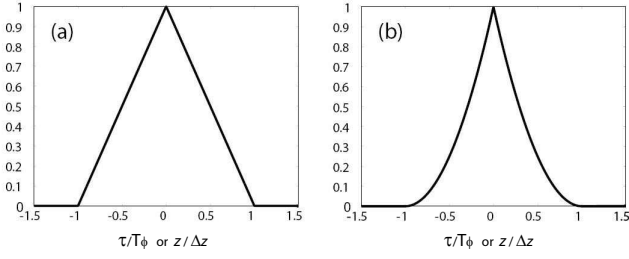


Fig. 2. Plot of correlation function $g_1(\tau)$ (a), and its square $g_1^2(\tau)$ (b). The horizontal axis units is either τ/T_Φ (for time correlation), or $z/\Delta z$ with $\Delta z = c_{US} T_\Phi$ (for z resolution).

make random jumps at time intervals of T_Φ , are periodic (pseudo random) with periodicity $T = NT_\Phi$, where $N = 2^{14}$ typically. In order to characterize the random phase sequence, one can introduce the phase correlation function g_1 [24]:

$$\begin{aligned} g_1(\tau) &= \langle e^{j\psi_P(t)} e^{-j\psi_P(t-\tau)} \rangle \\ &= \langle e^{j\psi_{US}(t)} e^{-j\psi_{US}(t-\tau)} \rangle \end{aligned} \quad (1)$$

Since $N \gg 1$, the correlation function $g_1(\tau)$ has a triangular shape whose Full Width at Half Maximum (FWHM) is T_Φ in time units, and $\Delta z = c_{US} T_\Phi$ in length units (see Fig. 2 (a)).

In order to choose the z selected zone in the sample, the phase ψ_P is delayed with respect to ψ_{US} in a way that

$$\psi_P(t) = \psi_{US}(t - \tau) \quad (2)$$

with $\tau = z/c_{US}$.

The signal detection procedure is the same as in reference [23]. In order to get a time varying signal on the photodiode PD, we apply on the US beam an extra $H(t) = \pm 1$ rectangular modulation signal at frequency $\omega_{mod}/2\pi = 1/T_{mod} = 3$ kHz, with duty cycle r . This frequency has been chosen to satisfy the condition of validity of theory (see Fig. 2 of reference [24]),

$$T_\Phi \ll T_{mod} \ll \tau_{PR}. \quad (3)$$

Other modulation frequencies are possible if Eq. 3 condition remains fulfilled. We have chosen to use here a ± 1 rectangular modulation, because this modulation is (i) easy to make, (ii) yields a quite good Lock-in signal, and (iii) has been considered in theory [23, 26].

Within the interval $t = 0$ to T_{mod} we have thus:

$$\begin{aligned} H(t) &= +1 \quad \text{for } 0 < t/T_{mod} < r \\ &= -1 \quad \text{for } r < t/T_{mod} < 1 \end{aligned} \quad (4)$$

The US beam is $H(t) = \pm 1$ modulated by using a second DBM in an AM modulator configuration. A US signal at

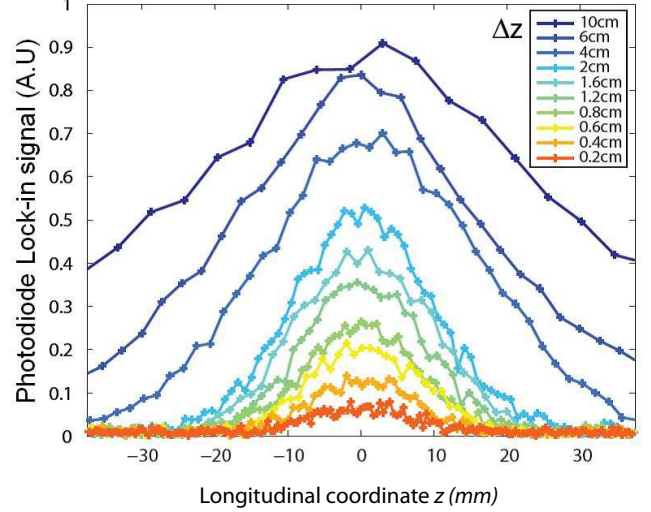


Fig. 3. Photodiode Lock-in acousto optic signal as a function of the longitudinal coordinate z for for $\Delta z = 10.0, 6.0, 4.0, 2.0, 1.6, 1.2, 0.8, 0.6, 0.4$ and 0.2 cm.

~ 2 MHz is fedded within the LO port of the DBM, while the $H(t)$ rectangular signal is fedded within the IF port. The $H(t)$ signal is generated by a computer driven signal generator, which controls the frequency $\omega_{mod}/2\pi$ and the duty cycle r . The ± 1 modulated US output is then obtained on the LO port. Since the modulation is fast with respect to the recording of the tagged photon grating on the PR crystal ($\omega_{mod} \gg 1/\tau_{PR}$), the modulated component of the index grating that is grooved in the PR crystal is proportional to $[(1 - 2r)r\text{sinc}(\pi r)]$ where r is the extra modulation duty cycle [26]. In order to maximize this component in the Lock-in detection, the duty cycle is fixed at $r = 0.24$.

The photodetector (PD) is a silicon photodiode (Hamamatsu S2386-8k, area $S_{PD} = 0.3$ cm²) connected to a home-made 10M Ω transimpedance amplifier. The modulated component of the Photodiode signal at ω_{mod} is measured by a Lock-in amplifier (EG&G Inc. 7210; integration time $\tau \simeq 100$ ms). We have stacked all the (sample+crystal+photodetector) together in order to optimize the detection flux without using lenses.

3. Quantitative study of the AOCT Point Spread Function (PSF) along z

Lesaffre et al. [24] have calculated the Point Spread Function (PSF) of the AOCT signal, and show that $\text{PSF}(z)$ is simply equal to g_1^2 expressed in length units. This function is plotted on Fig.2 (b), and corresponds to what expected in experiments. In order to measure $\text{PSF}(z)$, and to compare it with theory, we have plotted the photodiode Lock-In Signal S_{PD} as a function of the delay τ for phases sequences with different correlation times T_Φ . By this way, one can vary the location $z = c_{US}\tau$ of the selected zone, and the correlation length $\Delta z = c_{US}T_\Phi$.

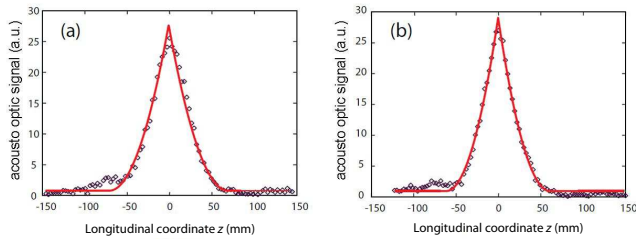


Fig. 4. Experimental profiles (black circles) made with $\Delta z = 10.0$ (a), and 6.0 cm (b). Theoretical shape g_1^2 (red curves) made by adjusting Δz in order to get the best fit with experiment. Fit yields $\Delta z = 10.27$ (a) and 6.09 cm (b).

The experiment is made with an *Agar + Intralipid* 10% phantom sample without absorbing inclusion. The reduced scattering coefficient is $\mu'_S = 10 \text{ cm}^{-1}$. The sample thickness is $L_y = 3$ cm along the illumination direction y . Other dimension are $L_x \times L_z = 6.5 \times 6.5 \text{ cm}^2$. The optical power is $P_S = 1 \text{ W}/1 \text{ cm}^2$ on the sample, while the reference beam on the GaAs crystal is $P_R = 600 \text{ mW}/0.32 \text{ cm}^2$. Acoustic pressure at maximum is $P_{max} = 1.6 \text{ MPa}$, and lock-in integration time is $\tau_c = 100$ ms.

Although the experiments presented in this paper use the same setup, they have been done at different time, with slightly different laser power and optical adjustments. The parameters P_S , P_R , P_{max} and τ_c may thus change from one experiment to the next. Similarly, the sample parameters: thickness L_y , lateral dimension L_x, L_z and scattering coefficient μ'_S may have changed, for good or bad reasons.

Figure 3 shows the Photodiode Lock-In signal as a function of z for Δz varying from 10 cm down to 0.2 cm. When Δz is small (0.6, 0.4 and 0.2 cm), the curve maximum is almost proportional to Δz , while the width remains nearly constant. The shape of the curves corresponds then to the shape, along z , of the cloud of photons that travel through the sample and that reach the Photodiode. In the region crossed by the US beam, the thickness of the cloud along x and z is about 1.5 cm i.e. $0.5 \times$ the thickness of the sample. When Δz is larger than the width of the cloud, i.e. for $\Delta z = 6$ and 4 cm, the curve maximum saturates, and the width increases linearly with Δz . In that last case, one can neglect the width of the cloud, and the $S_{PD}(z)$ corresponds to PSF(z).

To make a first quantitative test of theory [24], we have plotted both the measured acousto optic signal and the theoretical point spread function (PSF) g_1^2 . We have considered situation where the PSF width ($\Delta z = 10$ and 6 cm) is larger than the thickness of the cloud (about 1.5 cm). In such case, the experimental profile must be close to theoretical PSF g_1^2 . We have thus plotted g_1^2 (red curves of Fig. 4) by adjusting Δz in order to get the best fit with the experimental data. The

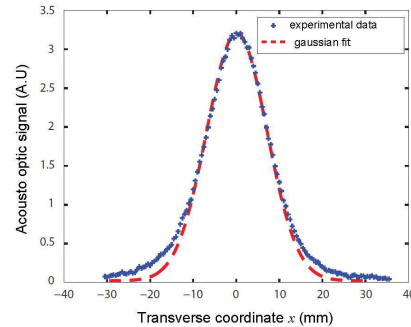


Fig. 5. Photodiode Lock-In signal S_{PD} as a function of the PZT location along the x axis. Experimental data (cross), and $\exp(-x^2/w_g^2)$ Fit with $w_g = 10.2$ mm (red dashed line).

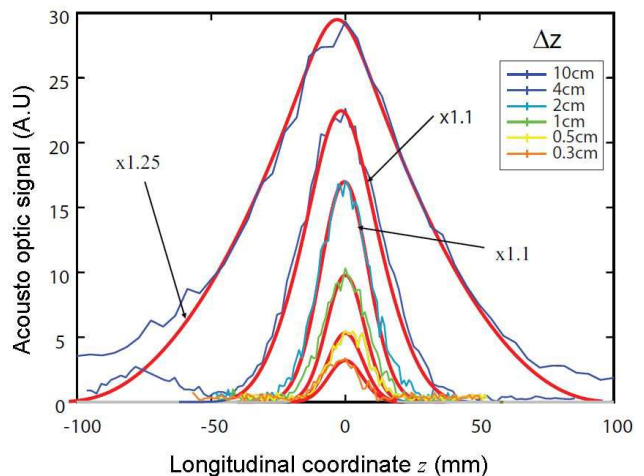


Fig. 6. Colored curves: experimental profiles $S_{PD}(z)$; Red curves: theoretical profiles $A g_1^2(x) \otimes \exp(-x^2/w_g^2)$ where \otimes is the convolution operator. Δz is 10, 4, 2, 1, 0.5 and 0.3 cm.

fit yields $\Delta z = 10.27$ and 6.09 (for the g_1^2 curves) in excellent agreement with $\Delta z = 10$ and 6 cm (experiments).

In order to compare the $S_{PD}(z)$ experimental curves with theory for any Δz , one has to calculate $g_1^2(z) \otimes C_z(z)$, where \otimes is the convolution operator, and $C_z(z)$ the shape of the cloud of photons along z . Since the cloud is symmetric with respect to the photon propagation direction y , the shapes C_x and C_z along x and z are the same. We have measured C_x by moving the PZT transducer along x with a step motor, and recorded the photodiode signal $S_{PD}(x)$ as a function of the PZT location x . $S_{PD}(x)$ is plotted on Fig.5.

We have assumed that $C_z(x) = C_x(x) = S_{PD}(x)$, and we approximate $C_x(x)$ by this gaussian fit $C_x(x) \simeq \exp(-x^2/w_g^2)$ with $w_g = 10.2$ mm (see Fig.5). Replacing $C_z(z)$ by the fit, we have calculated the theoretical profiles $A g_1^2(x) \otimes \exp(-x^2/w_g^2)$, where A is an arbitrary gain parameter that should be the same for all value of Δz .

To compare theory and experiment, we have adjusted the gain parameter A in order to get the best agreement. As mentioned on the curves of Fig. 6, we have slightly modified the gain parameter replacing A by $1.1 \times A$ for $\Delta z = 4$ and 2 cm, and by $1.25 \times A$ for $\Delta z = 10$ cm. This small change of the gain parameter is interpreted here as small drifts (laser power,...) yielding small changes of the experimental signal and/or detection efficiency during the several hours of data acquisition. We have displayed the theoretical and experimental profiles on Fig.6. The agreement is excellent.

The $S_{PD}(z)$ curves displayed on Fig. 4 and Fig. 6 exhibit two regimes. The first regime is observed when Δz is smaller than the width of the cloud of photons of Fig.5 i.e. for $\Delta z < 1.5$ cm. The width of the curve remains nearly constant, while the curve maximum is almost proportional to Δz . This is expected since in that case the width of the cloud is larger than PSF (i.e. for $\Delta z > 1.5$ cm). The shape of the curves corresponds then to the shape of the cloud along z . On the other hand, the AOCT signal (i.e. the area of the Fig. 3 curves) is ever proportional to the number of diffuser that contribute coherently to the AOCT signal (i.e. is proportional to Δz). As a consequence, since the width remains almost constant (and is equal to the width of the cloud), the maximum is proportional to Δz .

The second regime is observed when Δz is larger than the width of the cloud, i.e. for $\Delta z > 1.5$ cm. The curve maximum saturates, and the width increases linearly with Δz . This is expected since in that case the width of the cloud is smaller than PSF (i.e. for $\Delta z > 1.5$ cm). One can then neglect the width of the cloud, and the Fig. 3 curves corresponds to the width of PSF(z), which increases like Δz , and thus like the AOCT signal. The maximum of the signal then saturates.

4. AOCT images along the x and z directions.

AOCT has been used to obtain 2D images of different samples. The random phase jump time T_{Φ} is kept constant. The scan along z is made by varying the AOCT delay τ with $z = \tau C_{US}$. The scan along x is performed by moving the location x of the PZT transducer with a motor. In order to reduce the noise, the 2D acquired data are low pass filtered in the Fourier space with a cutoff frequency k_c .

A. Image of the cloud of Photon: sample without absorbing inclusion.

To validate the analysis of the PSF made in section 3, we have consider first a sample without inclusion in order to image the cloud of photons itself.

We have first imaged a sample without absorbing inclusion. The experiment is made with a $\mu'_s = 6 \text{ cm}^{-1}$ scattering sample, whose thickness is $L_y = 3.2$ cm, and whose dimensions are $L_x \times L_z = 6.5 \times 6.5 \text{ cm}^2$. The optical power is $P_S = 630 \text{ mW}/1 \text{ cm}^2$ on the sample, and $P_R = 650 \text{ mW}/0.32 \text{ cm}^2$ on the GaAs crystal. Acous-

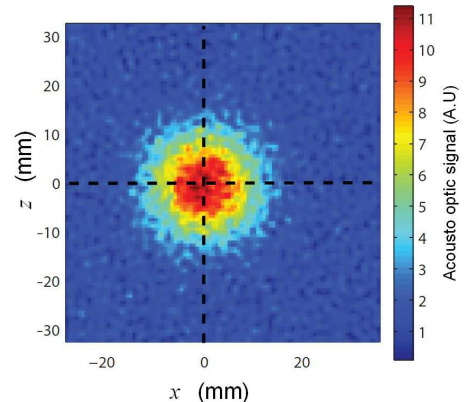


Fig. 7. AOCT image (x, z) of a scattering sample without absorbing inclusion ($e = 3.2 \text{ cm}$, $\mu'_s = 6 \text{ cm}^{-1}$).

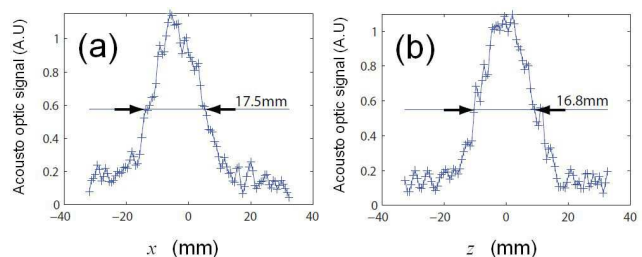


Fig. 8. Profiles of the AOCT photodiode lock-in signal of the sample of Fig.7 along x (a) and z (b) directions.

tic pressure is $P_{max} = 1.6 \text{ MPa}$, and lock-in integration time is $\tau_c = 100 \text{ ms}$. Steps along x and z are $\delta_x = 0.65 \text{ mm}$, and $\delta_z = 0.65 \text{ mm}$ yielding 100×100 pixels images. The jump time is $T_{\Phi} = 1.9 \mu\text{s}$ yielding $\Delta z = 2.9 \text{ mm}$. The data are low pass filtered in the Fourier space. The spatial cutoff frequency is $k_c = 1 \text{ mm}^{-1}$ for k_x and for k_z .

Figure 7 shows the xz image of the sample. Since there is no absorbing inclusion, we get an image of the cloud of photons that travel through the sample and that reach the photodiode. The US beam es the cloud, and the image corresponds to a cut of the cloud along the US beam z axis, and the PZT motion x axis. As shown on Fig.7 the cloud is symmetric by rotation around the y axis, exhibiting the same extension within the x and z direction as shown on Fig.8. This is expected since the x and z extension (17.5 and 16.8 mm) is much larger than the resolution along x (FWHM = 1.2 mm for the focused US beam) and z ($\Delta z = 2.9 \text{ mm}$).

B. Quantitative study of the z resolution in the high resolution case: images and cuts made with a low scattering sample ($\mu'_s \simeq 0$) with two absorbing inclusions.

To perform a quantitative study of the z resolution in the high resolution case (Δz down to 1.4 mm), we con-

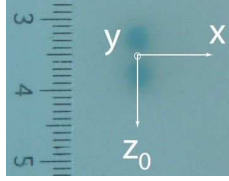


Fig. 9. Photographs of the non scattering sample ($e = 3.0$ cm, $\mu'_s = 0$) having 2 absorbing inclusions (diameter: 3 mm, spacing: 2 mm).

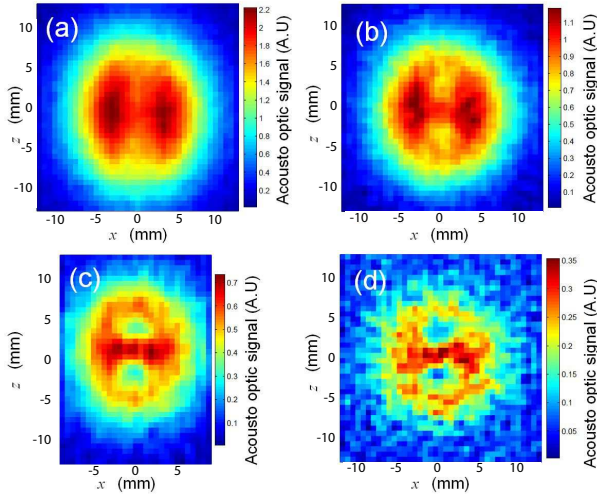


Fig. 10. AOCT xz images of the sample of Fig.9 with $\Delta z = 11.4$ mm (a), 5.7 mm (b), 2.9 mm (c) and 1.4mm (d).

considered a sample with two absorbing inclusions of known geometry. These inclusions were made by Agar Agar with the addition of India ink drops. They have a cylindrical shape (diameter: 3 mm, length 5 mm), separated by 2 mm, and oriented along y direction (see Fig.9). In practice, the absorption coefficient was not properly measured but was considered as high. We considered a low scattering sample with Agar Agar and without intralipid. This has been done to get a better sensitivity at high resolution, (since the AOCT signal is proportional to Δz) and to avoid shadow effect. Indeed, the density of photons near an absorbing inclusion is lower than expected, because the diffused photons that travel through the sample may have crossed or will cross the absorbing zone. The scattering coefficient μ'_s is nevertheless non zero (as seen on the image of Fig. 9) yielding a photon diffusion cloud, whose size is not well known. Since AOCT is based on the detection of diffuse light, a diffuser (sheet of white paper) is placed at the outlet of sample. The experimental conditions are: $P_S = 1$ W/ 1 cm² on the sample; $P_R = 630$ mW/0.32 cm² on the crystal; $P_{max} = 1.6$ MPa; $\tau_c = 100$ ms; $k_c = 1$ mm⁻¹.

We have studied the z resolution by imaging the sample and by plotting vertical cuts for Δz varying from

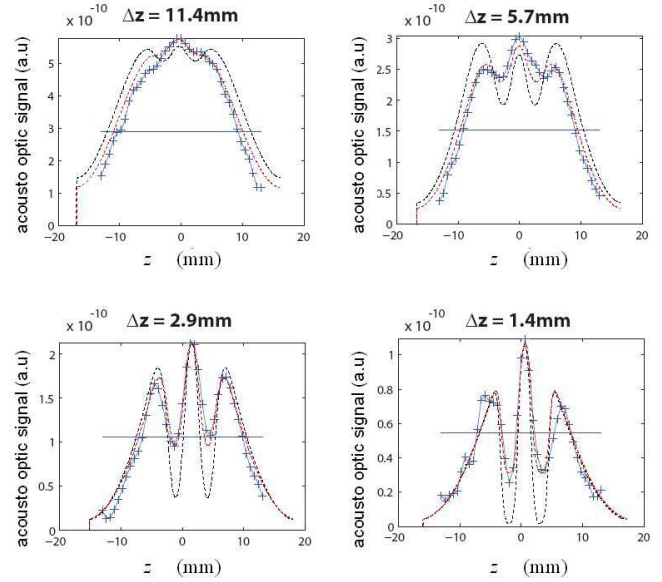


Fig. 11. Profiles of the AOCT photodiode lock-in signal (crosses and blues curves) of the sample of Fig.9 along z direction with $\Delta z = 11.4$ mm (a), 5.7 mm (b), 2.9 mm (c) and 1.4mm (d), and theoretical profiles (dashed line curves) calculated with totally (black) and partially (red) absorbing inclusions.

11.4 mm to 1.4 mm. The images are displayed on Fig.10 with $\Delta z = 11.4$ mm (a), 5.7 mm (b), 2.9 mm (c) and 1.4 mm (d). Figure 11 presents their axial profiles along the vertical axis connecting the two inclusions (crosses and solid blue curves). On the image corresponding to $\Delta z = 11.4$ mm (a), we cannot distinguish any inclusion. We just see a decrease of the signal along the vertical column. For $\Delta z = 5.7$ mm (b), the inclusions are seen, but the contrast is low. Changing to $\Delta z = 2.9$ mm (c), the two inclusions are clearly resolved, but the contrast is not yet optimum. The latter is maximum for $\Delta z = 1.4$ mm (d), but the signal becomes quite low, especially near the absorbing inclusion. Image (d) is thus noisy. Typically, the best compromise between resolution and amplitude is obtained when the resolution is comparable to the dimensions of the object, that is to say for $\Delta z = 2.9$ mm compared to the diameter of the inclusion of 3mm. We can also notice from image (a) to (d) that the acousto-optic signal decreases linearly with Δz .

In order to compare the experimental results to theory, we have also plotted on Figure 11 the theoretical profiles $S_{PD}(z)$ (dashed curves). The calculation of $S_{PD}(z) = g_1^2(z) \otimes C_z(z)$ is made by considering that the density of photons $C_z(z)$ within the inclusions is either zero (black dashed curves) or attenuated by a factor 0.3 (red dashed curves) with respect to the density within the cloud. Moreover, the gaussian profile of the cloud ($\exp(-x^2/w_g^2)$) is supposed to be a little narrower than in section 3 ($w_g = 8.0$ in place of 10.2 mm). As seen on Fig. 11, the imaging contrast obtained in experiment is

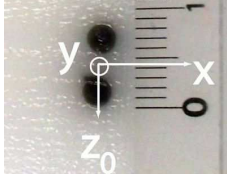


Fig. 12. Pictures of the diffusing sample ($e = 2$ cm, $\mu'_s = 10\text{cm}^{-1}$) with two absorbing (3 mm diameter, 2 mm spacing) at mid-thickness in the plane (yz).

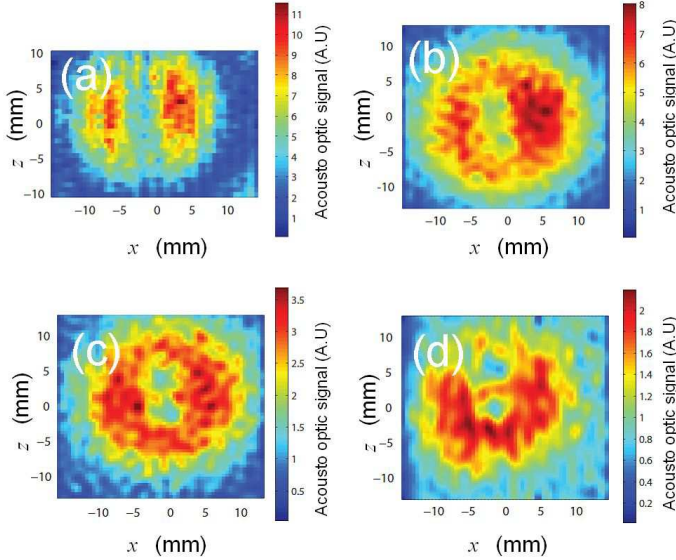


Fig. 13. AOCT xz images of the sample of Fig.12 with $\Delta z = 11.4$ mm (a) , 5.7 mm (b) , 2.9 mm (c) and 1.4 mm (d).

lower than the one expected for totally absorbing inclusions (black dashed curves). This effect can be related to the imperfect absorption of the inclusion. By considering a finite absorption of 0.3, the agreement of the experiment with theory is much better (red dashed curves).

C. Sample with two absorbing inclusions

To illustrate how Δz affects the image quality on a more realistic situation, we have imaged a scattering sample with two absorbing inclusions, whose are similar to those used in section B. These inclusions were made by the same mix of Agar Agar+Intralipides than the rest of the sample, with the addition of India ink drops. They have a cylindrical shape (diameter: 3 mm, length 5 mm), separated by 2 mm, and oriented along y direction (see Fig.9). The sample thickness is $L_y = 2$ cm, with a scattering coefficient $\mu'_s = 10\text{cm}^{-1}$. Two inclusions of 3mm diameter are oriented along the y direction and are spaced 2 mm (see Fig.12). The experimental conditions are: $P_S = 350$ mW/ 1 cm^2 on the sample; $P_R = 650$ mW/ 0.32 cm^2 on the crystal; $P_{max} = 1.6$ Mpa; $\tau_c = 100$ ms; $k_c = 1\text{ mm}^{-1}$.

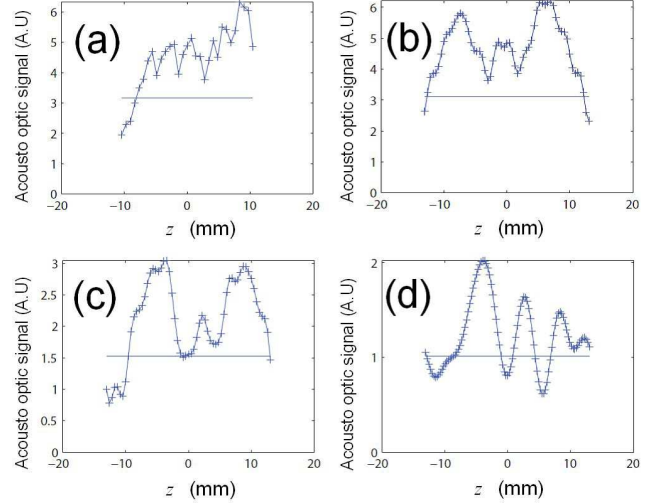


Fig. 14. Profiles of the acousto optic AOCT photodiode lock-in signal of the sample of Fig.12 along z direction with Δz of 11.4 mm (a), 5.7 mm (b), 2.9 mm (c) and 1.4 mm (d).

Figure 13 shows the experimental images obtained for $\Delta z = 11.4$ mm, 5.7 mm, 2.9 mm and 1.4 mm. Figure 14 shows the corresponding vertical cut along z , at the center of the sample. For $\Delta z = 11.4$ mm, we do not discern any inclusion, but only a decrease in the signal at the center of the sample that informs us that it is probably one or more absorbing inclusion. For $\Delta z = 5.7$ mm, both inclusions are discernible. This is accentuated for $\Delta z = 2.9$ mm and 1.4 mm. We can briefly compare these images in scattering medium to those performed in the non-diffusing in section B.

For $\Delta z = 2.9$ mm, the inclusions are less visible here with scattering ($\mu'_s = 10\text{cm}^{-1}$), than without scattering ($\mu'_s = 0$). This can be interpreted as a shadow effect that can occur in scattering medium. Here again, we can also notice that the signal decreases linearly with Δz .

As in the section B, the best compromise between resolution and amplitude is obtained when the resolution is comparable to the dimensions of the object, that is to say for $\Delta z = 2.9\text{mm}$ compared to the diameter of the inclusion of 3mm.

5. Conclusion

In this paper, we have confirmed that the Lesaffre et al. [23] AOCT technique is able to bring z resolution to acousto optic imaging. We have presented new experimental results, and we have studied how the z resolution depends on the jumping time T_ϕ , or on the correlation length Δz . By working at low resolution, we have performed a quantitative comparison of the measured z shape with the theoretical one, and we have shown by this way that the theoretical expression of the AOCT Point Spread Function of reference [24] agrees with experiments.

We have imaged samples with 2 absorbing inclusion (3 mm diameter, 2 mm spacing) embedded within 2 different samples (diffusing or not). The non diffusing sample has been used to analyse the resolution and to compare it quantitatively with theory in the high resolution regime ($\Delta z = 1.4$ and 2.9 mm). The experimental resolution agrees with theory. The scattering sample has been considered to get qualitative images closer to what expected in living sample. The resolution varies similarly with Δz but is slightly lower. We have interpreted this decreased resolution as a shadow effect.

The non-scattering sample permits to validate the model by avoiding the problem of shadow effect which will tend to decrease the resolution. The corresponding images permit a quantitative analysis of the resolution in the case of a weak scattering sample with a good signal to noise ratio. Otherwise, the study with a high scattering sample show more realistic results, but in return more qualitative because the resolution is limited by the signal to noise ratio and the shadow effect.

Note that the experiments have been done here with *Agar + Intralipid* phantoms, and not with ex-vivo tumor tissues because phantoms are easier to prepare, and because their optical properties (absorption and reduced scattering coefficients μ'_s) are more reproducible, and can be thus more precisely measured. The experimental analysis done here correspond to AOCT experiments made with photorefractive detection of the acousto optic signal [23], which have been theoretically analyzed by Lesaffre et al. [24]. We did not try to analyse in detail the recent AOCT experiments made with holographic detection of the acousto optic signal [27] because the corresponding theory has not been published yet. Moreover, the comparison of the figure of merit of the two detection schemes (photorefractive versus holographic) in a clinical in vivo application has not been done.

In order to use the AOCT technique for biomedical applications, as for example to get information on breast tumors, it is necessary to work with thicker scattering samples (> 5 cm), while respecting the acoustic biomedical standards. In practice, this is very difficult to realize at $\lambda = 1064$ nm because of water absorption. On the other hand, experiments realized within the optical therapeutic window - i.e. around $\lambda = 800$ nm - are easier because the absorption is lower and therefore the transmitted signal much bigger. This change of optical wavelength involves the use of other photorefractive crystals (as SPS:Te, ZnTe, BSO) whose development is in progress [21,28]. Besides, the biomedical safety recommendations concern both the optical and acoustical powers [29,30]. For the optical power, the limit is 1W per cm at $\lambda = 1064$ nm for optical continuous emission, and all the experiments in this paper follow the standard. The acoustic power standards concern the peak to peak acoustic power and the average acoustic power. The first one requires a maximum instantaneous power of 190 W/cm², corresponding to a maximum pressure of 2.5 MPa in water. All the experiments in this

paper follow this first acoustic standard. The second acoustic standard requires an average acoustic power of 720 mW/cm². Because of the acoustic continuous emission of this set-up, this second acoustic is not reached. To satisfy this last standard, one could use the AOCT technique with long acoustic pulses (about 1 ms), which are compatible with the long pulse lasers already used in Ultrasound-modulated optical imaging [22]. These two modifications would allow the AOCT technique to be used with thicker samples, while respecting the acoustic biomedical standards.

This work was supported by funds from the French National Research Agency (ANR-2011-BS04-017-SIMI 4-ICLM).

References

1. W. Leutz and G. Maret. Ultrasonic modulation of multiply scattered light. *Physica B: Condensed Matter*, 204(1-4):14–19, 1995.
2. L. Wang, S.L. Jacques, and X. Zhao. Continuous-wave ultrasonic modulation of scattered laser light to image objects in turbid media. *Optics Letters*, 20(6):629–631, 1995.
3. M. Kempe, M. Larionov, D. Zaslavsky, and AZ Genack. Acousto-optic tomography with multiply scattered light. *Journal of the Optical Society of America A*, 14(5):1151–1158, 1997.
4. S. Leveque, A.C. Boccara, M. Lebec, and H. Saint-Jalmes. Ultrasonic tagging of photon paths in scattering media: parallel speckle modulation processing. *Optics Letters*, 24(3):181–183, 1999.
5. G. Yao and L.V. Wang. Theoretical and experimental studies of ultrasound-modulated optical tomography in biological tissue. *Applied Optics*, 39(4):659–664, 2000.
6. L. Wang and X. Zhao. Ultrasound-modulated optical tomography of absorbing objects buried in dense tissue-simulating turbid media. *Applied Optics*, 36(28):7277–7282, 1997.
7. M. Gross, P. Goy, and M. Al-Koussa. Shot-noise detection of ultrasound-tagged photons in ultrasound-modulated optical imaging. *Optics Letters*, 28(24):2482–2484, 2003.
8. F. Le Clerc, L. Collot, and M. Gross. Numerical heterodyne holography with two-dimensional photodetector arrays. *Optics Letters*, 25(10):716–718, 2000.
9. M. Gross and M. Atlan. Digital holography with ultimate sensitivity. *Optics Letters*, 32(8):909–911, 2007.
10. F. Verpillat, F. Joud, M. Atlan, and M. Gross. Digital Holography at Shot Noise Level. *Journal of Display Technology*, 6(10):455–464, 2010.
11. M. Gross, P. Goy, BC Forget, M. Atlan, F. Ramaz, AC Boccara, and AK Dunn. Heterodyne detection of multiply scattered monochromatic light with a multipixel detector. *Optics Letters*, 30(11):1357–1359, 2005.
12. M. Atlan and M. Gross. Spatiotemporal heterodyne detection. *JOSA A*, 24(9):2701–2709, 2007.
13. T.W. Murray, L. Sui, G. Maguluri, R.A. Roy, A. Nieva, F. Blonigen, and C.A. DiMarzio. Detection of ultrasound-modulated photons in diffuse media using the photorefractive effect. *Optics Letters*, 29(21):2509–2511, 2004.

14. L. Sui, R.A. Roy, C.A. DiMarzio, and T.W. Murray. Imaging in diffuse media with pulsed-ultrasound-modulated light and the photorefractive effect. *Applied Optics*, 44(19):4041–4048, 2005.
15. F. Ramaz, B. Forget, M. Atlan, AC Boccara, M. Gross, P. Delaye, and G. Roosen. Photorefractive detection of tagged photons in ultrasound modulated optical tomography of thick biological tissues. *Optics Express*, 12(22):5469–5474, 2004.
16. M. Lesaffre, F. Jean, F. Ramaz, AC Boccara, M. Gross, P. Delaye, and G. Roosen. In situ monitoring of the photorefractive response time in a self-adaptive wavefront holography setup developed for acousto-optic imaging. *Optics Express*, 15(3):1030–1042, 2007.
17. X. Xu, H. Zhang, P. Hemmer, D. Qing, C. Kim, and L.V. Wang. Photorefractive detection of tissue optical and mechanical properties by ultrasound modulated optical tomography. *Optics Letters*, 32(6):656–658, 2007.
18. A. Lev and BG Sfez. Pulsed ultrasound-modulated light tomography. *Optics Letters*, 28(17):1549–1551, 2003.
19. A. Lev, E. Rubanov, B. Sfez, S. Shany, and AJ Foldes. Ultrasound-modulated light tomography assessment of osteoporosis. *Optics Letters*, 30(13):1692–1694, 2005.
20. M. Atlan, BC Forget, F. Ramaz, AC Boccara, and M. Gross. Pulsed acousto-optic imaging in dynamic scattering media with heterodyne parallel speckle detection. *Optics letters*, 30(11):1360–1362, 2005.
21. S. Farahi, G. Montemezzani, A.A. Grabar, J.P. Huignard, and F. Ramaz. Photorefractive acousto-optic imaging in thick scattering media at 790 nm with a $\text{Sn}_2\text{P}_2\text{S}_6:\text{Te}$ crystal. *Optics Letters*, 35(11):1798–1800, 2010.
22. G. Rousseau, A. Blouin, and J.P. Monchalain. Ultrasound-modulated optical imaging using a powerful long pulse laser. *Optics Express*, 16(17):12577–12590, 2008.
23. M. Lesaffre, S. Farahi, M. Gross, P. Delaye, C. Boccara, and F. Ramaz. Acousto-optical coherence tomography using random phase jumps on ultrasound and light. *Optics Express*, 17(20):18211–18218, 2009.
24. M. Lesaffre, S. Farahi, AC Boccara, F. Ramaz, and M. Gross. Theoretical study of acousto-optical coherence tomography using random phase jumps on ultrasound and light. *JOSA A*, 28(7):1436–1444, 2011.
25. T.Y. Chang, A.E. Chiou, and P. Yeh. Cross-polarization photorefractive two-beam coupling in gallium arsenide. *Journal of the Optical Society of America B*, 5(8):1724–1729, 1988.
26. M. Gross, F. Ramaz, B. Forget, M. Atlan, A. Boccara, P. Delaye, and G. Roosen. Theoretical description of the photorefractive detection of the ultrasound modulated photons in scattering media. *Optics Express*, 13(18):7097–7112, 2005.
27. E. Benoit a la Guillaume, S. Farahi, E. Bossy, M. Gross, and F. Ramaz. Acousto-optical coherence tomography with a digital holographic detection scheme. *Optics Letters*, 37(15):3216–3218, 2012.
28. S. Farahi, A.A. Grabar, J.P. Huignard, and F. Ramaz. Time resolved three-dimensional acousto-optic imaging of thick scattering media. *Opt. Lett.*, 37:2754–2756, 2012.
29. Medical electrical equipment : Particular requirements for the safety of ultrasound diagnostic and monitoring equipment, iec 60601 part 2-37.
30. Information for manufacturers seeking marketing clearance of diagnostic ultrasound systems and transducers. division of reproductive, abdominal, ear, nose, throat and radiological devices, food and drug administration, 1997.